N-doped carbon dots decorated 3D g-C$_3$N$_4$ for visible-light driven peroxydisulfate activation: Insights of non-radical route induced by Na$^+$ doping

Xiaomei Liu [a], Jun Wang [a], Di Wu [a], Zhe Wang [b], Yang Li [a,c], Xiaobin Fan [a,c], Fengbao Zhang [a], Guoliang Zhang [a], Wenchao Peng [a,c,*]

[a] School of Chemical Engineering and Technology, Tianjin University, Tianjin 300350, China
[b] Division of Environment and Sustainability, The Hong Kong University of Science and Technology, Hong Kong Special Administrative Region of China
[c] Chemistry and Chemical Engineering Guangdong Laboratory, Shantou 515031, China

ARTICLE INFO

ABSTRACT

A novel material with N-doped carbon dots decorated three-dimensional graphitic carbon nitride (NCDs/TCN) is synthesized using NaCl as template. Abundant Na$^+$ are found to be in-situ doped in 3D g-C$_3$N$_4$ framework. Experiments and density functional theory (DFT) calculations suggest that peroxydisulfate (PDS) activation follows radical and non-radical pathways on the NCDs/TCN catalyst. NCDs have superior up-conversion photoluminescence property and can enhance charge separation efficiency, thus improving the photocatalytic reactivity of 3D g-C$_3$N$_4$ and promoting the radical activation of PDS efficiently. Interestingly, the NCDs/TCN-PDS* complex can be formed due to the large adsorption energy of doped Na$^+$ for PDS, thus inducing the non-radical PDS activation pathway. This work provides an effective approach to combine radical and non-radical pathways for boosting PDS activation and gives deep insights for the non-radical pathway induced by doped Na$^+$ in 3D g-C$_3$N$_4$.

1. Introduction

The sulfate radicals-based advanced oxidation process (SR-AOP), as an emerging advanced oxidation processes (AOPs), has attracted considerable attention on account of its strong ability to degrade refractory organic pollutants in wastewater remediation [1]. In this process, persulfate, including peroxydisulfate (PDS) and peroxymonosulfate (PMS), can be activated by ultrasound, electricity, alkali, heat, or various of catalysts to produce sulfate radicals (SO$_4^{\bullet-}$) with high redox potential (2.5–3.1 eV) [2–5]. In recent years, light driven SR-AOP is booming due to its low cost and energy conservation, in which the persulfate is usually activated by the photo-separated electrons and holes generated from photocatalytic semiconductors [6–8].

Graphitic carbon nitride (g-C$_3$N$_4$) as a metal-free semiconductor has exhibited a prominent potential for persulfate activation due to its low cost, facile synthesis and high stability [7,9]. To date, the activation mechanism of persulfate by catalysts includes radical pathway and non-radical pathway, while non-radical pathway includes ^{1}O$_2$,

high-valent metal-oxo species-dominated mechanism, and direct electrons transfer process [10,11]. Under light irradiation, persulfate usually undergoes activation to initiate radical-mediated oxidation reactions on g-C$_3$N$_4$-based materials [7]. Integrating non-metals or transition metals into g-C$_3$N$_4$ can regulate the electronic structure of pristine g-C$_3$N$_4$, persulfate activation with ^{1}O$_2$ or high-valent metal-oxo species-dominated non-radical pathway can thus be achieved [10,12]. However, the direct electrons transfer process for persulfate activation based on g-C$_3$N$_4$ materials has rarely been reported. Thus, it's highly desirable to gain more in-depth investigations for the direct electrons transfer process of persulfate activation based on g-C$_3$N$_4$-based materials. Moreover, radical pathway or non-radical pathway usually occurs independently, resulting in low persulfate activation efficiency. Combining radical and non-radical pathways together for persulfate activation might be a more effective way to remove organic pollutants.

Conventional g-C$_3$N$_4$ shows limited catalytic activity for persulfate activation due to its small surface area, low visible-light utilization efficiency, and rapid charge carrier recombination [13,14]. Different approaches, including morphology control [14,15], heteroatom doping [7,

[16], heterojunction construction [17,18], defect engineering [19], and composing with other materials [20], have been used to enhance the catalytic activity of g-C_3N_4. N-doped carbon dots (NCDs) have been widely employed to integrate with semiconductors to improve the photo-activity [21–23]. It's worth noting that NCDs can inhibit the recombination of photo-separated charges, which can also improve the utilization ratio of visible light via its superior up-conversion photo-luminescence (PL) property [22,24]. Therefore, to modify g-C_3N_4 with NCDs may increase its adsorption range for visible light and separation ability for electron-hole pairs, thus achieving enhanced photo-activity. Additionally, compared to the conventional synthesis of g-C_3N_4, introducing templates during g-C_3N_4 synthesis is also a very effective and facile way for obtaining more active g-C_3N_4. SiO_2 is widely employed as template to synthesize porous g-C_3N_4 [8,25], however, the removal of SiO_2 template by corrosive and toxic chemicals (NH_4HF_2 or HF) is not safety and green. NaCl crystal as a green and safety template has been widely concerned [26–28]. The materials synthesized with NaCl template can have 3D structure with improved specific surface area and enhanced active sites exposure [29,30]. Moreover, Na^+ can be in-situ doped in 3D g-C_3N_4 [26], however, the effects of doped Na^+ in 3D g-C_3N_4 for persulfate activation mechanism has never been discussed and remains unclear.

Herein, NaCl is used as template to synthesize NCDs/TCN material with porous and micro-cage morphology. XPS and solid NMR technologies are used to characterize the chemical structure of NCDs/TCN. The catalytic performance of NCDs/TCN is evaluated with sulfamethoxazole (SMX) as model pollutant and PDS as additive oxidant under visible light irradiation. The degradation mechanism of this catalytic system is investigated via quenching experiments, electrochemical tests, in-situ Raman spectra and electron spin resonance (EPR) measurements. Moreover, DFT calculations are also applied to unravel the deeply reasons for its degradation mechanism.

2. Experiments

2.1. Materials synthesis

2.1.1. Synthesis of TCN

TCN was synthesized using a calcination method with NaCl crystal as template. Typically, dicyandiamide (DCDA) and NaCl with different molar ratios were dissolved in 100 mL water. After a 20 h frozen treatment, the ice content was completely removed in a lyophilizer to obtain a white fluffy powder. Subsequently, the white powder was placed in a crucible wrapped with tin foil and calcinated at 550 °C for 4 h under N_2 atmosphere. The obtained yellow powder was then washed with water thoroughly to remove NaCl template and then freeze-dried. The final yellow samples synthesized with different molar ratios of DCDA and NaCl (DCDA: NaCl=1:5, 1:10, and 1:15) were denoted as TCN (1:5), TCN (1:10), and TCN (1:15). Unless otherwise stated, the used sample for characterizations and reaction was TCN (1:10) (marked as TCN). Additionally, bulk g-C_3N_4, denoted as BCN, was synthesized by the calcination of DCDA at 550 °C for 4 h under N_2 atmosphere.

2.1.2. Synthesis of NCDs

N-doped carbon dots (NCDs) were synthesized by a hydrothermal method [24]. Typically, 1.0 g urea and 3.0 g citric acid were dissolved in 15 mL water. The mixture was then placed in a Teflon-sealed autoclave and heated at 180 °C for 5 h. The obtained brown solution was centrifuged at 10,000 rpm for 30 min to remove the large particles. Subsequently, the solution was adjusted to neutral pH with HCl solution, which was then dried at 70 °C to obtain the NCDs powder. Finally, the powder was fully suspended in water to obtain a 20 g/L solution.

2.1.3. Synthesis of NCDs/TCN

The TCN decorated with different percentages of NCDs (NCDs/TCN) were synthesized using the same procedure for TCN synthesis with the as-prepared NCDs solution as the solvent (Fig. 1a). Besides, NCDs/BCN sample with BCN as support was synthesized by the same procedure.

3. Results and discussion

3.1. Materials characterization

The synthesis process of NCDs decorated TCN with NaCl as template is shown in Fig. 1a. The suspension of NCDs is firstly obtained using a hydrothermal method, which is then used to decorate the in-situ generated TCN. Due to the solubility of NaCl, it can be removed easily by a water washing process. As shown in Fig. S1a, the BCN sample shows stacked bulk structure. Contrastively, the materials synthesized with NaCl template display 3D staggered network structure (Fig. S1b-d), which is favorable for light harvesting due to multiple photonic reflection and the slow-photon effect [31,32]. The obtained white fluffy powders (NaCl @ NCDs/DCDA) present smooth surface, indicating DCDA is intimately coated on the surface of NaCl template (Fig. S1e). After calcination, the yellow powder (NaCl @ NCDs/TCN) without removing NaCl shows rough surface (Fig. S1f). In Fig. 1b-d, the NCDs/TCN sample also exhibits 3D staggered network structure, remaining the morphology of NaCl crystal. As shown in Fig. 1e, NCDs (red circles) are successfully deposited on the surface of TCN, and the characteristic lattice spacing of NCDs (0.24 nm) (inset of Fig. 1e) can be observed, corresponding to the (100) lattice plane of graphite [33]. The energy-dispersive spectroscopy (EDS) elemental mapping images corresponding to Fig. 1f are shown in Fig. 1g-j, and all of the C, N, O, and Na elements are evenly distributed.

The N_2 adsorption-desorption isotherms and corresponding pore size distribution of the as-prepared materials are measured and shown in Fig. S2a, b. Typical type IV isotherms with type H3 hysteresis loop are observed for all samples, indicating their mesoporous structure. Compared to BCN (8.87 m^2/g), TCN sample (46.38 m^2/g) possesses larger specific surface areas (SSA), indicating that employing NaCl as template can increase the SSA of BCN effectively. Interestingly, compared to TCN, the NCDs/TCN shows much higher SSA (95.81 m^2/g) due to the alleviation of excessive g-C_3N_4 layer stacking and generation of porous structure after NCDs decoration. In Fig. S2c, the diffraction peaks of as-prepared samples correlate well with the PDF#87–1526 of g-C_3N_4. The BCN shows graphitic stacking structures with two characteristic peaks at 13.0° and 27.3°, which correspond to the (100) plane of in-plane periodic tri-s-triazine units and the (002) plane of interlayer stacking of aromatic structures, respectively [34]. The (100) plane of TCN and NCDs/TCN samples almost disappeared, attributing to the damage of in-plane long-range order structure [35]. After decorating with NCDs, the characteristic peaks of NCDs are not observed for NCDs/TCN due to the low loading and uniform distribution of NCDs. Fourier transform infrared (FI-IR) spectra (Fig. S2d) of all samples show typical absorption at 807 cm^{-1}, 1200–1800 cm^{-1}, and 3000–3660 cm^{-1}, corresponding to the bending vibration of triazine units, the stretching vibration modes of C-N heterocycles, and the stretching of -OH and -NH_x, respectively [36,37]. A new peak at around 2180 cm^{-1} is observed for TCN and NCDs/TCN materials, which can be assigned to the vibration of cyano (-C≡N) [38,39], indicating cyano groups can be introduced into g-C_3N_4 molecular structure with NaCl as template. Additionally, two extra bands at 1000 cm^{-1} and 1156 cm^{-1} can be found, reflecting that hydroxyl groups (-OH) might be grafted on g-C_3N_4 [40].

XPS is employed to characterize the surface compositions of materials (Fig. 2). Fig. 2a depicts that all samples show C 1s, N 1s, and O 1s signals. TCN and NCDs/TCN also contain Na 1s peak (Table S1), which indicates that the doped Na^+ might exist in TCN framework. As plotted in Fig. 2b, three peaks located at 284.8 eV, 286.4 eV, and 288.3 eV are observed for all samples, corresponding to surface adventitious carbon (C-C/C=C), C-OH, and sp^2-hybridized carbon (N-C=N), respectively [40,41]. In Table S2, the C-OH content in TCN and NCDs/TCN is much
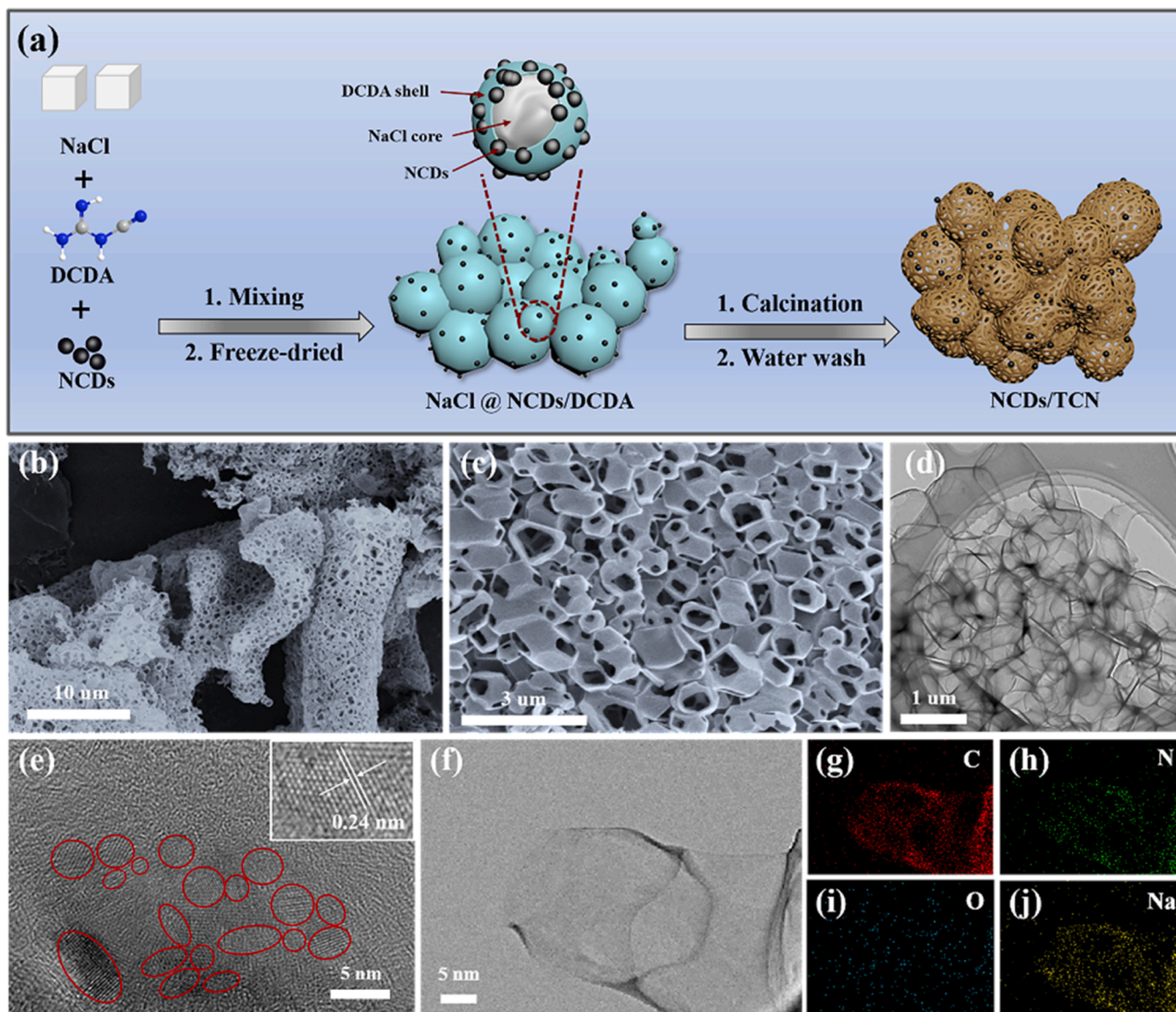
Fig. 1. Schematic diagram for the synthesis of the NCDs/TCN composite (a). SEM images (b, c), TEM image (d), HRTEM images (e, f), and EDS images (g-j) of NCDs/TCN sample.

higher than that in BCN. The low C-OH content in BCN may be ascribed to hydroxylated carbon atoms on the surface, and the obvious improved C-OH content in TCN and NCDs/TCN might be attributed to the generation of C-OH structure in 3D g-C_3N_4 matrix [40–42]. Moreover, the molecular structure is further investigated by solid-state ^{13}C NMR spectra (Fig. S3a). Compared with BCN, two new peaks at 167.6 ppm and 120.9 ppm are observed for NCDs/TCN, which are assigned to C-OH and -C≡N structure, respectively [9,40]. The N 1s spectra of all samples exhibit four peaks at 398.7 eV, 400.1 eV, 401.2 eV, and 404.4 eV (Fig. 2c), attributing to sp^2-hybridized nitrogen (C-N=C), tertiary nitrogen (N-C_3), -NH$_x$, and the charging effecting, respectively [8]. It's worth noting that compared with BCN, the C-N=C content in TCN and NCDs/TCN decreased (Table S2) and the C/N mol ratio increased (Table S1), indicating the introduction of NaCl may affect the condensation reaction of g-C_3N_4 and result in the loss of N in C-N=C structure. The N-C_3 content in TCN and NCDs/TCN increases obviously compared to BCN (Table S2), which might be attributed to the overlap of -C≡N peak, whose binding energy is very close with C-N=C and N-C_3 [37]. Owing to the electron-withdrawing groups (-C≡N) generation, the peak of N-C_3 in TCN and NCDs/TCN samples shifts to low binding energy (Table S2). As shown in Fig. 2d, in addition to surface adsorbed H$_2$O

(532.2 eV), another two new peaks at 531.5 eV and 535.0 eV are detected for TCN and NCDs/TCN, attributing to (N)$_2$C-OH structure and Na KLL Auger peak, respectively [8,37]. In Fig. 2e, a peak centered at 1071.4 eV is observed for TCN, which is in accordance with the reported binding energy of Na 1 s for NaN$_3$ [25], indicating the doping of Na atoms into carbon nitride structure. For NCDs/TCN sample, the binding energy of Na 1 s shifts to 1071.7 eV, which indicates the change of electron density around Na atoms due to the introduction of NCDs. Additionally, the content of Cl element in TCN and NCDs/TCN is in a trace scale, which might be ascribed to the incomplete removal of NaCl (Table S1). Based on the above analysis, it can be concluded that the N loss in C-N=C structure opens the s-triazine heterocycle of g-C_3N_4, which increases the amount of the O atoms (Table S1) due to the formation of -OH groups. The -C≡N group can be generated from the deprotonation of -C-NH$_2$. On the other hand, Na$^+$ are doped into the interstitial positions of g-C_3N_4 structure. Therefore, the plausible grafting sites of -C≡N and -OH groups as well as the doping sites of Na$^+$ in NCDs/TCN are tentatively proposed (Fig. S3b). Furthermore, the difference charge density (CDD) of TCN is shown in Fig. 2f. High density electrons are found around Na$^+$, which not only indicates the strong coordination interaction between Na and N atoms but also demonstrates
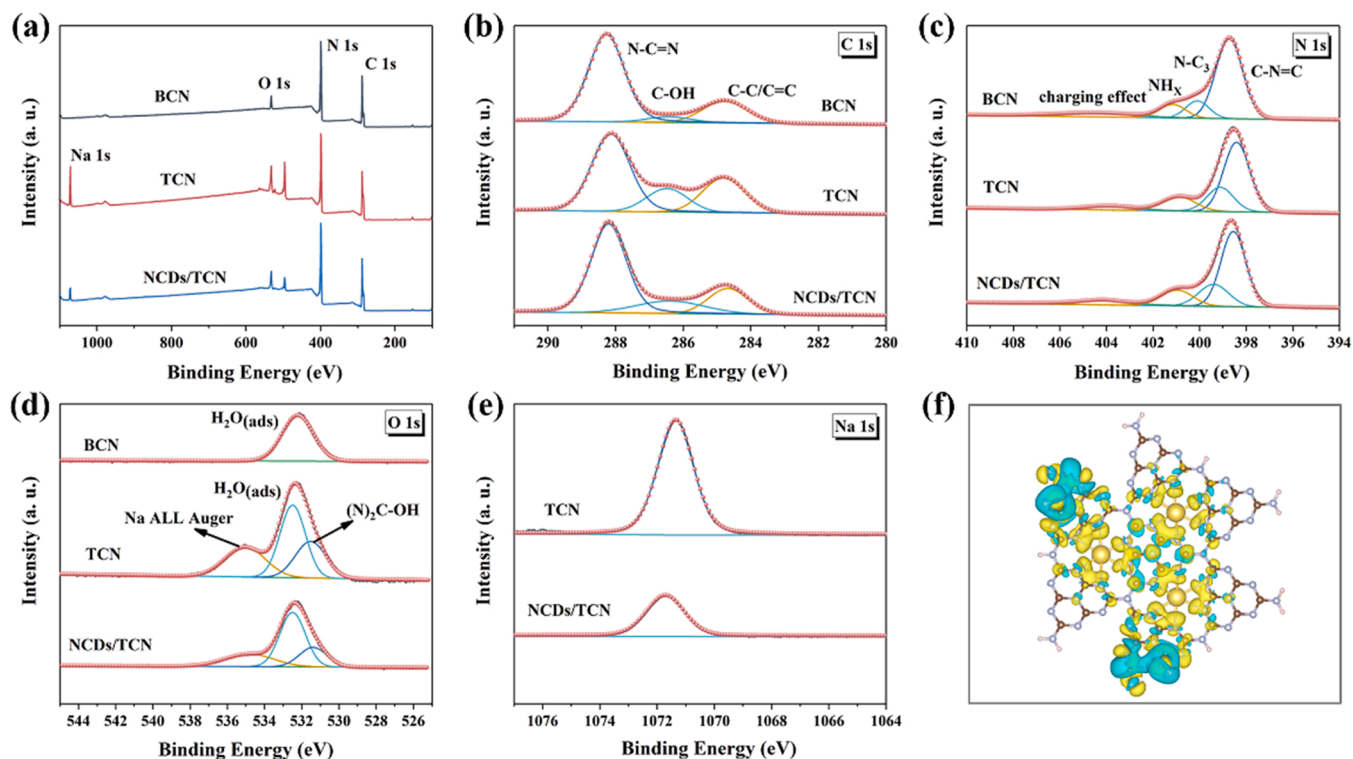
Fig. 2. XPS survey spectra (a), C 1s (b), N 1s (c), O 1s (c), and Na 1s spectra (e) of the as-obtained samples. The calculated charge density difference (CDD) of TCN (f), the yellow and blue areas denote charge accumulation and charge loss, respectively.

the possible electrons transfer pathway from g-C_3N_4 to Na^+ sites.

3.2. Optical and photoelectrochemical properties

The optical properties of BCN, TCN, and NCDs/TCN are characterized by UV–vis DRS (Fig. 3a). NCDs/TCN sample exhibits the strongest absorption in the ultraviolet-visible range (300–800 nm). Compare with

TCN, an obvious red shift of NCDs/TCN can be found after NCDs modification, suggesting that NCDs can broaden the visible light spectral response. Furthermore, the up-converted PL property of NCDs is investigated by the PL measurement. As shown in Fig. 3b, NCDs can absorb long wavelength light (600–900 nm) and then emit short wavelength light (440–500 nm). Especially, with the light of 700–800 nm input, 500–600 nm light can also be emitted, implying that NCDs can enhance
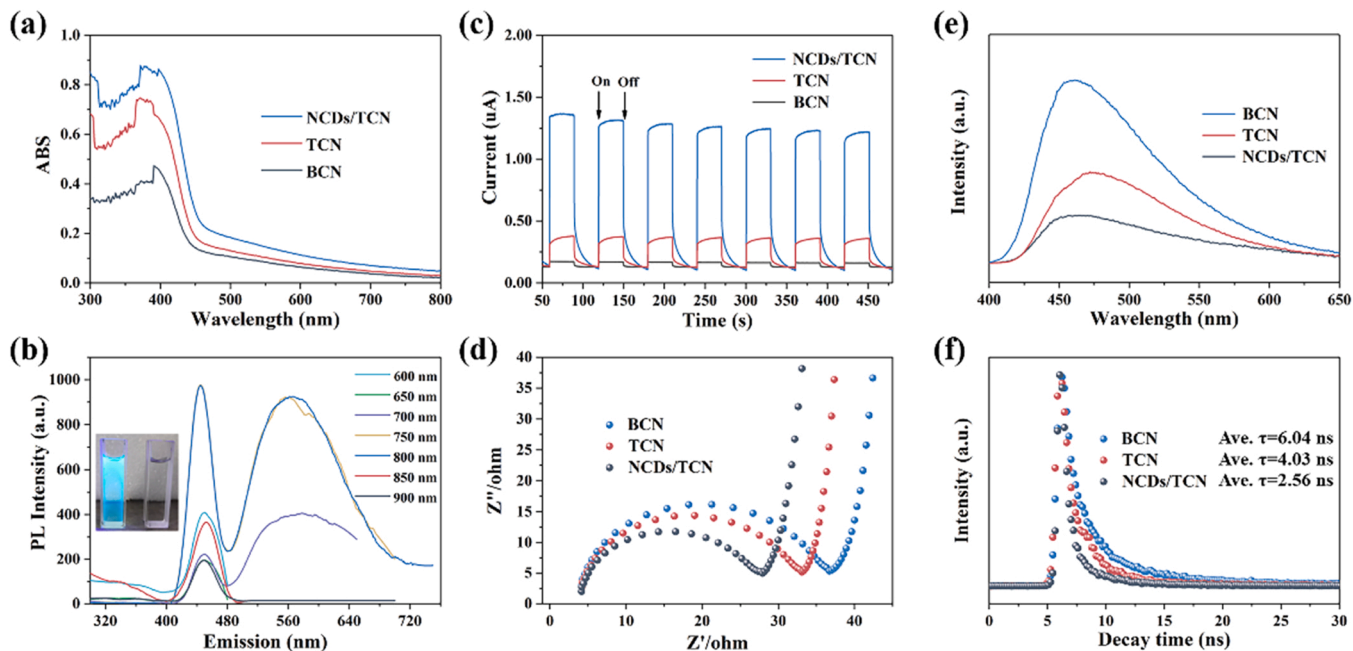

Fig. 3. UV–vis DRS (a). Up-converted PL spectra of the NCDs (b). Transient photocurrent responses (c), EIS Nyquist plots (d), PL spectra (e), time-resolved PL spectra (f) of BCN, TCN, and NCDs/TCN samples.

the light-harvesting capacity of TCN via the conversion of near-infrared excitation wavelength to visible light.

The photo-induced charge separation and transfer behaviors are then investigated by photoelectrochemical measurements. In Fig. 3c, the photocurrent response of TCN is higher than that of BCN, revealing the enhanced charge separation efficiency. Moreover, NCDs/TCN shows the strongest photocurrent intensity, indicating that NCDs modification can inhibit the charge recombination efficiently. Additionally, the electrochemical impedance spectroscopy (EIS) spectra (Fig. 3d) display that the impedance arc radius of NCDs/TCN is the smallest, suggesting the smallest resistance of NCDs/TCN for charge migration. PL spectra are further employed to confirm the separation rate of photo-induced electron-hole pairs. As shown in Fig. 3e, BCN displays the highest PL intensity, implying the fastest recombination rate of electron-hole pairs. Compared with TCN, the PL intensity of NCDs/TCN sample is lower, thus further proving the enhanced charge separation by the decoration of NCDs. The emission peaks of BCN, TCN, and NCDs/TCN are at 458 nm, 469 nm, and 471 nm, respectively, which shows the same trend as the UV–vis DRS results. Time-resolved PL spectroscopy (Fig. 3f and Table S3) is also applied to investigate the charge separation dynamics. The average emission decay time of NCDs/TCN (2.56 ns) is much lower than BCN (6.04 ns) and TCN (4.03 ns), indicating that more photogenerated electrons in NCDs/TCN are involved in photocatalytic reactions rather than combined with photo-generated holes. Based on the photocurrent response, EIS, PL, and time-resolved PL spectra, it can be concluded that the photo-generated charge separation and transfer ability can be effectively improved by the introduction of NCDs on TCN.

3.3. Photocatalytic performance

The photocatalytic performance of as-prepared samples is evaluated with SMX as target pollutant and PDS as oxidant under visible light irradiation. Compared to BCN, all TCN based catalysts show better catalytic activity for SMX removal, TCN (1:10) with the smallest SSA however displays optimal photocatalytic performance for SMX degradation (Fig. S4), indicating SSA is not the primary factor for activity enhancement on these samples. Therefore, the TCN (1:10) is selected finally as support for NCDs decoration. The adsorption capacities of NCDs/TCN samples are investigated under dark condition. In Fig. S5a, the adsorption-desorption equilibrium is achieved within 30 min. It can be seen that ~18% SMX can be removed by adsorption. As shown in Fig. S5b, c, with increased loading content of NCDs, the photocatalytic activities of NCDs/TCN materials first increase and then decrease. Therefore, an appropriate amount of NCDs in NCDs/TCN photocatalyst is crucial for obtaining good performance, and 1.0% NCDs/TCN exhibits the best photocatalytic performance for SMX degradation. With small loading content of NCDs in NCDs/TCN, the up-converted PL property of NCDs cannot be fully utilized and photo-generated charge separation ability is relatively low, thus only obtaining limited photocatalytic efficiency of NCDs/TCN. On the other hand, the photosensitive sites and doped Na^+ sites on TCN may be covered by excessive NCDs, resulting in the catalytic activity decrease of NCDs/TCN and relatively low removal efficiency of SMX. Furthermore, the up-converted PL property of NCDs can also be confirmed by the photocatalytic degradation of SMX under long-wavelength light irradiation. As shown in Fig. S5d, ~45% SMX can be removed within 40 min by NCDs/TCN with PDS as oxidant under LED irradiation (10 W, 700–710 nm), indicating the effective utilization of long-wavelength light for PDS activation.

As shown in Fig. 4a, TCN+PDS+dark system shows comparable SMX degradation performance to NCDs/TCN+PDS+dark system. Therefore, the NCDs are not active sites for chemical-catalytic driven PDS activation for SMX degradation under dark condition. Compared with TCN+Vis system, the removal efficiency of SMX on NCDs/TCN+Vis is obviously increased with a k value of 0.015 min^{-1}. Decoration by NCDs can therefore effectively promote the photocatalytic activity of NCDs/TCN, attributing to the enhanced utilization of visible light and separation of charge carriers. However, the degradation rate of SMX is still unsatisfactory by NCDs/TCN+Vis. Interestingly, the k values of TCN+PDS+Vis and NCDs/TCN+PDS+Vis systems are increased after the addition of PDS, and the system of NCDs/TCN+PDS+Vis exhibits remarkable catalytic activity for SMX degradation with a k value of 0.071 min^{-1} (Fig. S6). Moreover, ~84% of PDS can be consumed in the NCDs/TCN+PDS+Vis system (Fig. S7a). As shown in Fig. S7b, the total organic carbon (TOC) removal reaches 71.77% within 120 min, demonstrating that most of SMX can be degraded into harmless substances (CO_2 and H_2O) in this system. The catalytic activity of NCDs/
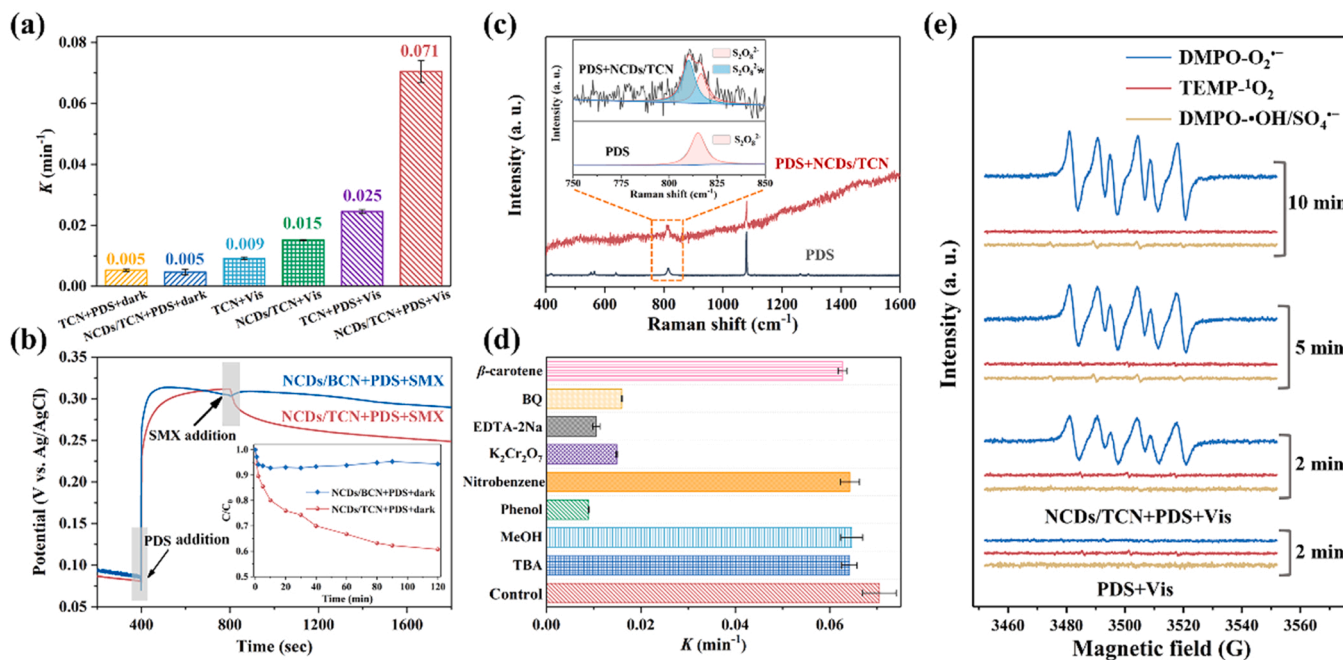

Fig. 4. The k values for different reaction systems (a). OCP curves (b). In situ Raman spectra of PDS and PDS+NCDs/TCN in the liquid solution (c). The k values of NCDs/TCN+PDS+Vis system under different scavengers (d). EPR spectra of $SO_4^{\bullet-}$, $\bullet$OH, $O_2^{\bullet-}$ and $^1O_2$ in different systems (e).

TCN outperforms those values of previously reported catalysts (Table S4).

It's worth noting that the photo-catalytic PDS activation process cannot occur in the NCDs/TCN+PDS+dark system, therefore, the degradation mechanism for SMX in NCDs/TCN+PDS+dark system might be attributed to chemical-catalytic driven PDS activation process [7]. In order to explore the degradation mechanism in NCDs/TCN+PDS+dark system, electrochemical measurements including linear sweep voltammetry (LSV) and open-circuit potential (OCP) are employed to study the electron-transfer process. In Fig. S8a, the current response of NCDs/TCN is slightly enhanced with the sole addition of PDS or SMX in the electrolyte. However, the current response is significantly intensified with simultaneous additions of PDS and SMX, suggesting that the co-presence of electron donor (SMX) and electron acceptor (PDS) enhances the non-radical pathway. As shown in Fig. 4b, the OCP of NCDs/BCN and NCDs/TCN electrodes are elevated immediately after PDS addition. It's speculated that PDS can interact with the catalyst to form catalyst-PDS* complex, which elevates the potential of the catalysts due to the partial electron transfer from the catalyst to PDS [1]. Compared with NCDs/BCN electrode, obvious potential decrease with SMX addition can be observed for NCDs/TCN electrode, indicating the electron-transfer process from SMX to the NCDs/TCN-PDS* complex. Moreover, compared to NCDs/BCN+PDS+dark system, NCDs/TCN+PDS+dark system displays better SMX degradation performance (inset of Fig. 4b). Therefore, non-radical pathway plays a very important role with NCDs/TCN as catalyst. In-situ Raman spectroscopy is further performed to confirm the formation of metastable NCDs/TCN-PDS* complex. As shown in Fig. 4c, the characteristic peak at 814 cm^{-1} ascribes to $S_2O_8^{2-}$ in PDS solution. After adding NCDs/TCN into PDS solution (inset of Fig. 4c), a new peak ($S_2O_8^{2-}$ *) at around 810 cm^{-1} is observed, which attributes to the bending vibrations of the prolonged O-O bond in the metastable NCDs/TCN-PDS* complex [43, 44].

3.4. Photocatalytic mechanism

The active species for SMX degradation in the NCDs/TCN+PDS+Vis system are explored by quenching tests (Figs. 4d and S9). MeOH is selected to scavenge $SO_4^{\bullet-}$ and •OH (k (MeOH, $SO_4^{\bullet-}$) = 3.2×10^7 M^{-1}s^{-1}, k (MeOH, •OH) = 9.7×10^8 M^{-1}s^{-1}). TBA is employed to selectively quench •OH (k (TBA, •OH) = 3.8–7.6 $\times 10^8$ M^{-1}s^{-1}) [45]. Both MeOH and TBA scavengers show slight inhibition on SMX removal, indicating that the $SO_4^{\bullet-}$ and •OH in reaction solution are not the primary active species for SMX oxidation (Fig. 4d). Previous studies reported that the generated radicals attached on the surface of catalysts cannot be quenched by MeOH and TBA [46]. While phenol can quench $SO_4^{\bullet-}$ and •OH on the catalyst surface effectively due to its weak polarity and the high reaction rate with $SO_4^{\bullet-}$/•OH. As depicted in Figs. 4d and S9a, with phenol addition, the SMX removal efficiency is reduced to 54%, indicating that $SO_4^{\bullet-}$ and •OH may be generated on the catalyst surface. It's reported that the reaction rate of nitrobenzene with •OH is much higher than that of $SO_4^{\bullet-}$ [46]. Therefore, the effect of •OH on the catalyst surface can be evaluated by adding nitrobenzene. Compared to phenol, nitrobenzene shows no significant effect on SMX degradation (Fig. 4d), indicating that $SO_4^{\bullet-}$ adsorbed on the catalyst surface plays an important role for this photocatalytic degradation system.

The contribution of photo-generated electrons and holes are investigated with $K_2Cr_2O_7$ and EDTA-2Na as quenchers, respectively (Figs. 4d and S9b). About 23.0% SMX can be suppressed when $K_2Cr_2O_7$ is added into the system, and the corresponding k value decreases from 0.071 min^{-1} to 0.015 min^{-1}. EDTA-2Na can also inhibit the degradation of SMX with a k value of 0.010 min^{-1} (Fig. 4d). These results suggest that both photo-generated electrons and holes in NCDs/TCN catalysts contribute to SMX removal. Moreover, BQ and β-carotene are used to evaluate the contribution of $O_2^{\bullet-}$ and $^1O_2$, respectively (Figs. 4d and S9b). When BQ is added into this photocatalytic system, 32.0% of SMX

can be suppressed and the k value is reduced to 0.016 min^{-1}, suggesting that $O_2^{\bullet-}$ is responsible for SMX decomposition. However, it can be seen that β-carotene shows negligible inhibit effect for SMX removal, proving the weak contribution of $^1O_2$. Previous studies have revealed that the $O_2^{\bullet-}$ can not only be generated from the reaction of dissolved oxygen and photo-generated electrons but also can be derived from $SO_4^{\bullet-}$ [7, 47]. In order to explore the origin of $O_2^{\bullet-}$, NCDs/TCN+PDS+Vis system is degassed with N_2 (Fig. S9b). However, SMX removal is slightly restrained, indicating $O_2^{\bullet-}$ is not produced from the reaction of dissolved oxygen and photo-generated electrons in this system. Additionally, the CB position of NCDs/TCN catalyst (−0.38 eV) is slightly negative than the redox potential of $O_2/O_2^{\bullet-}$ (−0.33 eV) (Fig. S15d), which also suggests that the limited thermodynamic available of photo-generated electrons for O_2 reduction. Moreover, N_2 +BQ displays comparable SMX inhibit effect (0.011 min^{-1}) to BQ (0.016 min^{-1}), proving that $O_2^{\bullet-}$ is derived from $SO_4^{\bullet-}$ not from the reaction of dissolved oxygen with photo-generated electrons.

EPR measurement is further employed to detect these active species with 5,5-Dimethyl-1-pyrroline N-oxide (DMPO) and 2,2,6,6-tetra-methyl-4-piperidinol (TEMP) as the spin-trapping agents. As shown in Fig. 4e, no EPR signals of DMPO-•OH/$SO_4^{\bullet-}$, DMPO-$O_2^{\bullet-}$ and TEMP-$^1O_2$ are observed in PDS+Vis system after two minutes reaction. The signals of DMPO-•OH/$SO_4^{\bullet-}$and TEMP-$^1O_2$ in NCDs/TCN+PDS+Vis system cannot be found with reaction time increasing. Relatively, the signal of DMPO-$O_2^{\bullet-}$ is clearly detected in the EPR spectrum, and the signal intensity continually increases during the reaction, indicating that $O_2^{\bullet-}$ as main active species contributes to SMX decomposition. EPR measurement cannot detect the signals of active species on catalyst surface. Most of $SO_4^{\bullet-}$ might be therefore adsorbed on the surface of NCDs/TCN, which is consistent with the results of surface radicals quenching experiments (Fig. S9a). These results indicate that the $SO_4^{\bullet-}$ on NCDs/TCN catalyst surface can react with water molecules to produce •OH, which can release into the reaction solution and transform into $O_2^{\bullet-}$ rapidly. In Fig. S9c, compared to the NCDs/TCN+Vis system, the signal intensity of DMPO-$O_2^{\bullet-}$ in NCDs/TCN+PDS+Vis system is increased obviously, further confirming that $O_2^{\bullet-}$ is derived from $SO_4^{\bullet-}$.

Density functional theory (DFT) calculation is further employed to investigate SMX degradation mechanism in NCDs/TCN+PDS+Vis system at the molecular level (Fig. 5). From characterization section, -OH and -C≡N groups are present at the edges of 3D g-C$_3$N$_4$ structure, and Na$^+$ is doped into the interstitial position of 3D g-C$_3$N$_4$. Three possible structures exist in NCDs/TCN catalyst are therefore simulated. As shown in Figs. 5a, S10a and b, both -OH, -C≡N, and Na$^+$ are existed in NCDs/TCN, PDS prefers to adsorb on Na$^+$ sites and the corresponding adsorption energies (E$_{ads}$) are very low (E$_{ads}$ < −0.5 eV). In order to investigate the influence of -OH and -C≡N groups on the adsorption of PDS at Na$^+$ sites, the models without -OH and -C≡N groups are established (Figs. 5b and S10c). It can be seen that these models also show strong PDS adsorption, suggesting that the -OH and -C≡N groups have no effects on PDS adsorption at Na$^+$ sites. Previous work reported that the strong adsorption of PDS by catalysts is more likely to form a strongly bonded and activated complex, giving rise to a non-radical pathway [48]. Therefore, the PDS is preferentially adsorbed on the Na$^+$ doped regions in NCDs/TCN catalyst, and the activation of PDS follows a non-radical pathway.

In the non-radical pathway, PDS bonds with NCDs/TCN catalyst to form a surface activated complex, which is capable of oxidizing SMX via a direct electron transfer through the 3D g-C$_3$N$_4$ matrix. The difference of SMX degradation efficiency between NCDs/BCN+PDS+dark and NCDs/TCN+PDS+dark reflects that Na$^+$ doping leads to the non-radical pathway and contributes to SMX degradation (inset of Fig. 4b). Moreover, comparable catalytic activities for SMX degradation can be achieved by NCDs/TCN+PDS+dark system and TCN+PDS+dark system, further confirming that the doped Na$^+$ rather than NCDs as active sites facilitate the non-radical pathway. In the quenching tests (Fig. S9b and
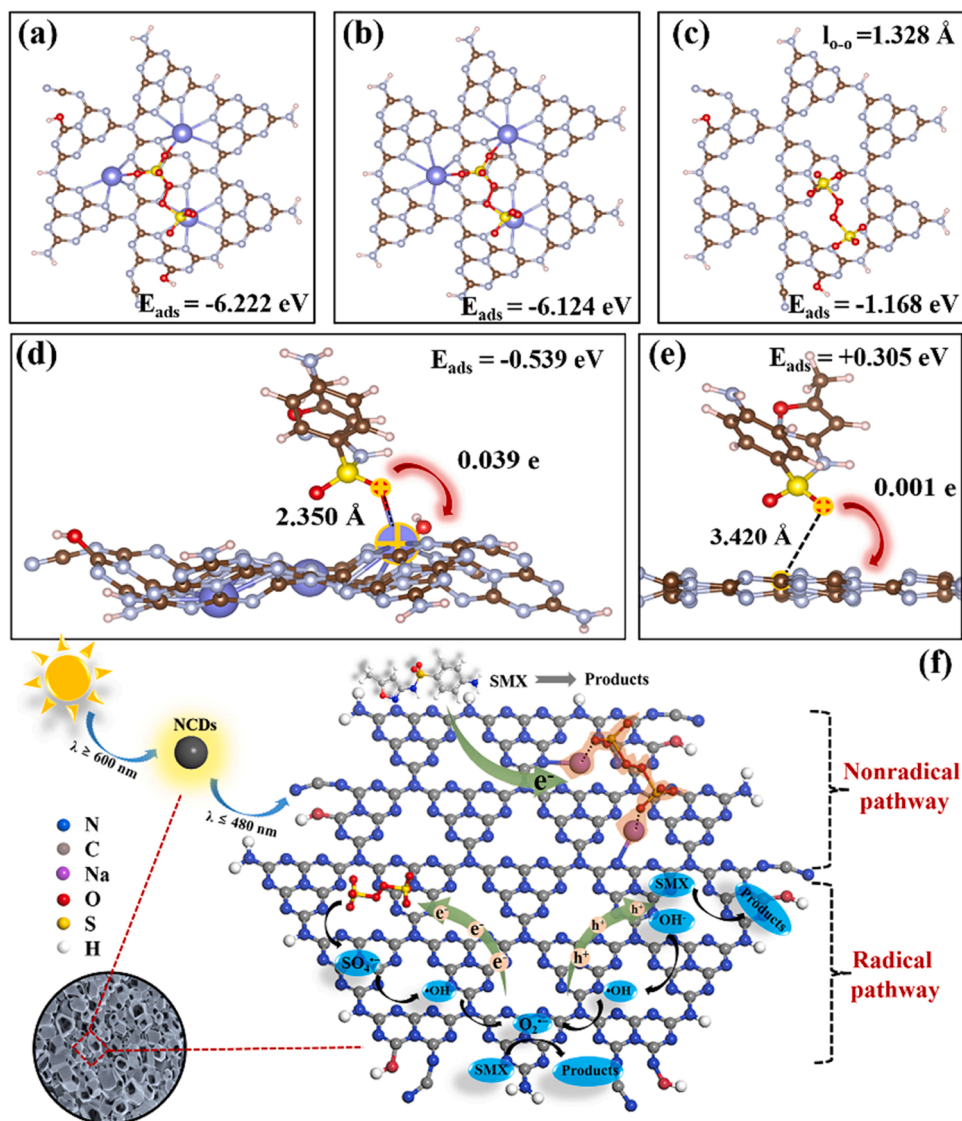
Fig. 5. Optimized adsorption geometric structures. (a) PDS adsorbed on 3D g-C$_3$N$_4$. (b) PDS adsorbed on 3D g-C$_3$N$_4$ without -OH and -C$\equiv$N groups. (c) PDS adsorbed on 3D g-C$_3$N$_4$ without Na$^+$ sites. SMX adsorbed on 3D g-C$_3$N$_4$ (d) and bulk g-C$_3$N$_4$ (e). PDS activation mechanism on NCDs/TCN catalyst (f).

Table S5), when the main active species (O$_2^{\bullet-}$ and h$^+$) are scavenged by BQ and EDTA-2Na, SMX also can be degraded by ~47%, reflecting the role of non-radical pathway. Excellent pollutants adsorption performance of catalysts promotes the non-radical process. The optimized adsorption configurations of SMX molecule on 3D g-C$_3$N$_4$ and bulk g-C$_3$N$_4$ are depicted in Fig. 5d, e. The E$_{ads}$ value of $-$ 0.539 eV for SMX on 3D g-C$_3$N$_4$ is much lower than on bulk g-C$_3$N$_4$ (+0.305 eV), indicating that SMX prefers to adsorb on 3D g-C$_3$N$_4$. The complex shows a distance of 2.350 Å between the SMX with 3D g-C$_3$N$_4$, which is much closer than that with bulk g-C$_3$N$_4$ (3.420 Å). Additionally, the calculated charge transfer values of SMX on 3D g-C$_3$N$_4$ and bulk g-C$_3$N$_4$ are 0.039 e and 0.001 e, respectively, suggesting that the affinity and charge transfer activity of 3D g-C$_3$N$_4$ is superior to those of bulk g-C$_3$N$_4$.

For the non-radical process, the electrons transfer pathway is further deeply studied by Bader charge calculation. It can be found that the charge on the tris-s-triazine ring of g-C$_3$N$_4$ decreases, and the charge on the doped Na$^+$ increases obviously, which confirms the electrons transfer pathway from g-C$_3$N$_4$ framework to Na$^+$ sites (Fig. S11a). When PDS is adsorbed on 3D g-C$_3$N$_4$, the number of electron transfer from the catalyst to PDS is about 0.772 (Fig. S11b). Thus, an electron transfer pathway from the tris-s-triazine ring of g-C$_3$N$_4$ to PDS will be formed

using the doped Na$^+$ as a bridge. When SMX pollutant is adsorbed on 3D g-C$_3$N$_4$ catalyst, the electrons of SMX are easy to lose and transferred to doped Na$^+$ sites via π-conjugated structure of g-C$_3$N$_4$. The electrons gathered on doped Na$^+$ will be further transferred to PDS. Therefore, combining the DFT results with experiments, the formation of NCDs/TCN-PDS* complex contributes to SMX oxidation according to the electrons transfer pathway.

When the adsorption of PDS on Na$^+$ sites reach saturation, the PDS will be adsorbed on the regions of 3D g-C$_3$N$_4$ without Na$^+$. The E$_{ads}$ are $-$ 1.168 eV and $-$ 1.038 eV in Figs. 5c and S10d, respectively. Compared with bulk g-C$_3$N$_4$ (E$_{ads}$ = $-$0.179 eV, Fig. S10e), the models of 3D g-C$_3$N$_4$ with -OH and -C$\equiv$N groups display higher adsorption energy for PDS, which indicates that the -OH and -C$\equiv$N groups may change the charge density distribution of 3D g-C$_3$N$_4$ and further affect PDS adsorption. The moderate E$_{ads}$ values of these models are favorable for radicals' generation, because smaller energy will be needed to break the interaction between PDS and catalysts. Moreover, compared with initial PDS (1.319 Å), the l$_{O-O}$ of adsorbed PDS are 1.328 Å (Figs. 5c) and 1.331 Å (Fig. S10d). The prolonged O-O bond is easier to cleave to generate SO$_4^{\bullet-}$ species, thus facilitates the PDS activation via radical pathway. According to the above analysis, PDS can be activated both by

non-radical and radical pathways on NCDs/TCN catalyst.

Based on the DFT calculations and experimental results, a possible PDS activation mechanism on NCDs/TCN catalyst is therefore proposed (Fig. 5f). Both non-radical pathway and radical pathway are existed on NCDs/TCN catalyst for PDS activation. For non-radical pathway, PDS is adsorbed on Na^+ sites to form NCDs/TCN-PDS* complex. Subsequently, the adsorbed SMX can be oxidized by losing electrons to the activated NCDs/TCN-PDS* complex (Eq. (S3)). When the Na^+ sites are occupied by PDS, the remaining PDS in the system will be activated via radical pathway. For radical pathway, continuous conversion of radicals on NCDs/TCN catalyst surface can be observed. Firstly, the NCDs as energy conversion units deposited on 3D $g-C_3N_4$ can effectively improve the utilization of visible light via its superior up-conversion PL property. Then, photogenerated electron-hole pairs can be produced on NCDs/TCN catalyst under visible light irradiation. The electron-hole pairs can be separated efficiently due to NCDs decoration. The separated electrons can be captured by PDS adsorbed on NCDs/TCN catalyst to produce $SO_4^{\bullet-}$ (Eq. (S4)). Then, $SO_4^{\bullet-}$ adsorbed on catalyst surface will react with H_2O to form $\bullet OH$ (Eq. (S5)). Moreover, the holes on valence band possess high oxidation potential (2.07 eV, Fig. S15d), which can not only oxidize SMX directly but also is thermodynamic available for OH^- oxidation, $\bullet OH$ can thus be generated from Eq. (S6) as well. The obtained $\bullet OH$ can be released into reaction solution and transformed into $O_2^{\bullet-}$ rapidly (Eqs. (S7)–(S9)). A small amount of $O_2^{\bullet-}$ can also be formed via Eqs. (S10) and (S11). Therefore, $O_2^{\bullet-}$ and h^+ are proved to be the main active species for SMX degradation in the NCDs/TCN+PDS+Vis system (Eq. (S12)).

3.5. Environmental implications

To investigate the application potential of this catalytic system, various factors existing in actual wastewater are considered. As shown in Fig. S12a, although $H_2PO_4^-$ slows down the SMX degradation due to $\bullet OH$ and $SO_4^{\bullet-}$ consumption, the anions including NO_3^-, Cl^-, and HCO_3^- show no inhabitation effect on SMX degradation, indicating that NCDs/TCN+PDS+Vis system can adapt to a more complex water environment. The influences of pH on SMX degradation are also studied (Fig. S12b). The photocatalytic activity is better in the alkaline environments (pH=9 and 11) than in the acidic environments (pH=2 and 5). However, it can also be seen that SMX is almost completely removed within 80 min in a wide initial pH range (2−11), implying that the treatment of industrial wastewater without pre-adjusting pH could become feasible. Additionally, NCDs/TCN+PDS+Vis system shows excellent degradation performance for other organic contaminants (Fig. S12c). Rhodamine B can be completely degraded within 10 min. The removal efficiencies of bisphenol A and 2, 4-dichlorophenol are 100% and 90% within 80 min, respectively. Moreover, under simulated sunlight, NCDs/TCN catalyst with PDS oxidant shows excellent degradation performance for SMX, and the corresponding k value reaches to 0.222 min^{-1} (Fig. S12d). Therefore, the removal efficiency of pollutants under sunlight is greatly improved, which shows great economic value and application potential in practical industrial wastewater treatment processes.

4. Conclusions

In summary, a novel metal-free NCDs/TCN photocatalyst was successfully synthesized by NaCl template method. Compared with BCN and TCN, NCDs/TCN catalyst shows optimal photocatalytic activity for SMX degradation with PDS as oxidant under visible light irradiation, which is 36.0 and 2.1 times faster than BCN and TCN, respectively. Based on DFT calculations and experiments, a radical generation ($O_2^{\bullet-}$) accompanied by a non-radical pathway is the key mechanism in the degradation of organic pollutions in NCDs/TCN+PDS+Vis system. The enhanced photocatalytic performance of NCDs/TCN is attributed to high visible light utilization and low charge recombination rate caused by NCDs. More importantly, the in-situ doped Na^+ is introduced by the presence of NaCl template. The doped Na^+ has strong adsorption ability for PDS, thus leading to the non-radical activation route. This work unveils the effects of doped Na^+ on the activation routes tuning of PDS, thus could provide useful theory for new catalysts synthesis with controllable catalytic abilities.

CRediT authorship contribution statement

Liu Xiaomei: Conceptualization, Methodology, Investigation, Writing – original draft. **Wang Jun:** Formal analysis, Visualization. **Wu Di:** Validation, Software. **Wang Zhe:** Writing – review & editing. **Li Yang:** Writing – review & editing. **Fan Xiaobin:** Writing – review & editing. **Zhang Fengbao:** Writing – review & editing. **Zhang Guoliang:** Writing – review & editing. **Peng Wenchao:** Resources, Conceptualization, Writing – review & editing, Supervision, Data curation.

Declaration of Competing Interest

The authors declare that they have no known competing financial interests or personal relationships that could have appeared to influence the work reported in this paper.

Supporting information

Additional details on the reagents, analytical data, calculation methods, and other associated supplementary texts, tables, and figures.

Appendix A. Supporting information

Supplementary data associated with this article can be found in the online version at doi:10.1016/j.apcatb.2022.121304.

References

[1] J. Wang, B. Li, Y. Li, X.B. Fan, F.B. Zhang, G.L. Zhang, W.C. Peng, Facile synthesis of atomic Fe-N-C materials and dual roles investigation of Fe-N$_4$ sites in Fenton-like reactions, Adv. Sci. 8 (2021) 2101824.

[2] S.Y. Yang, P. Wang, X. Yang, L. Shan, W.Y. Zhang, X.T. Shao, R. Niu, Degradation efficiencies of azo dye Acid Orange 7 by the interaction of heat, UV and anions with common oxidants: persulfate, peroxymonosulfate and hydrogen peroxide, J. Hazard. Mater. 179 (2010) 552–558.

[3] R.L. Yin, W.Q. Guo, H.Z. Wang, J.S. Du, X.J. Zhou, Q.L. Wu, H.S. Zheng, J. Chang, N.Q. Ren, Enhanced peroxymonosulfate activation for sulfamethazine degradation by ultrasound irradiation: performances and mechanisms, Chem. Eng. J. 335 (2018) 145–153.

[4] D. Wu, W.Y. Song, L.L. Chen, X.G. Duan, Q. Xia, X.B. Fan, Y. Li, F.B. Zhang, W. C. Peng, S.B. Wang, High-performance porous graphene from synergetic nitrogen doping and physical activation for advanced nonradical oxidation, J. Hazard. Mater. 381 (2020) 121010.

[5] D. Wu, Y. Zhao, Q. Xia, X.B. Fan, Y. Li, G.L. Zhang, F.B. Zhang, W.C. Peng, Bamboo-like nitrogen-doped carbon nanotubes on iron mesh for electrochemically-assisted catalytic oxidation, J. Hazard. Mater. 408 (2021) 124899.

[6] Y.L. Song, L. Huang, X.J. Zhang, H.Z. Zhang, L. Wang, H. Zhang, Y.L. Liu, Synergistic effect of persulfate and g-C$_3$N$_4$ under simulated solar light irradiation: implication for the degradation of sulfamethoxazole, J. Hazard. Mater. 393 (2020) 122397.

[7] X.M. Liu, Y. Li, X.B. Fan, F.B. Zhang, G.L. Zhang, W.C. Peng, Photo-accelerated Co^{3+}/Co^{2+} transformation on cobalt and phosphorus co-doped g-C$_3$N$_4$ for Fenton-like reaction, J. Mater. Chem. A 9 (2021) 22399–22409.

[8] S. Zhang, S. Song, P.C. Gu, R. Ma, D.L. Wei, G.X. Zhao, T. Wen, R. Jehan, B.W. Hu, X.K. Wang, Visible-light-driven activation of persulfate over cyano and hydroxyl group co-modified mesoporous g-C$_3$N$_4$ for boosting bisphenol A degradation, J. Mater. Chem. A 7 (2019) 5552–5560.

[9] L. Chen, C. Chen, Z. Yang, S. Li, C.H. Chu, B.L. Chen, Simultaneously tuning band structure and oxygen reduction pathway toward high-efficient photocatalytic hydrogen peroxide production using cyano-rich graphitic carbon nitride, Adv. Funct. Mater. 31 (2021), 2105731.

[10] F. Chen, L.L. Liu, J.J. Chen, W.W. Li, Y.P. Chen, Y.J. Zhang, J.H. Wu, S.C. Mei, Q. Yang, H.Q. Yu, Efficient decontamination of organic pollutants under high salinity conditions by a nonradical peroxymonosulfate activation system, Water Res. 191 (2021), 116799.

[11] B.H. Liu, W.Q. Guo, W.R. Jia, H.Z. Wang, Q.S. Si, Q. Zhao, H.C. Luo, J. Jiang, N. Q. Ren, Novel nonradical oxidation of sulfonamide antibiotics with Co (II)-doped g-C3N4-activated peracetic acid: role of high-valent cobalt-oxo species, Environ. Sci. Technol. 55 (2021) 12640–12651.

[12] F. Wu, H.W. Huang, T.F. Xu, W.Y. Lu, N. Li, W.X. Chen, Visible-light-assisted peroxymonosulfate activation and mechanism for the degradation of pharmaceuticals over pyridyl-functionalized graphitic carbon nitride coordinated with iron phthalocyanine, Appl. Catal. B Environ. 218 (2017) 230–239.

[13] S. Patnaik, D.P. Sahoo, K. Parida, Recent advances in anion doped g-C3N4 photocatalysts: a review, Carbon 172 (2021) 682–711.

[14] Q.H. Liang, B.B. Shao, S.H. Tong, Z.F. Liu, L. Tang, Y. Liu, M. Cheng, Q.Y. He, T. Wu, Y. Pan, J. Huang, Z. Peng, Recent advances of melamine self-assembled graphitic carbon nitride-based materials: design, synthesis and application in energy and environment, Chem. Eng. J. 405 (2021), 126951.

[15] F. He, Z.X. Wang, Y.X. Li, S.Q. Peng, B. Liu, The nonmetal modulation of composition and morphology of g-C3N4-based photocatalysts, Appl. Catal. B Environ. 269 (2020), 118828.

[16] F. Chen, X.L. Wu, C.Y. Shi, H.J. Lin, J.R. Chen, Y.P. Shi, S.B. Wang, X.G. Duan, Molecular engineering toward pyrrolic N-Rich M-N4 (M = Cr, Mn, Fe, Co, Cu) single-atom sites for enhanced heterogeneous Fenton-like reaction, Adv. Funct. Mater. 31 (2021), 2007877.

[17] J. Bian, Z.Q. Zhang, J.N. Feng, M. Thangamuthu, F. Yang, L. Sun, Z.J. Li, Y. Qu, D. Y. Tang, Z.W. Lin, F.Q. Bai, J.W. Tang, L.Q. Jing, Energy platform for directed charge transfer in the cascade Z-scheme heterojunction: CO2 photoreduction without a cocatalyst, Angew. Chem. Int. Ed. 60 (2021) 20906–20914.

[18] Y.X. Geng, D.Y. Chen, N.J. Li, Q.F. Xu, H. Li, J.H. He, J.M. Lu, Z-Scheme 2D/2D α-Fe2O3/g-C3N4 heterojunction for photocatalytic oxidation of nitric oxide, Appl. Catal. B Environ. 280 (2021), 119409.

[19] C.F. Huang, Y.P. Wen, J. Ma, D.D. Dong, Y.F. Shen, S.Q. Liu, H.B. Ma, Y.J. Zhang, Unraveling fundamental active units in carbon nitride for photocatalytic oxidation reactions, Nat. Commun. 12 (2021) 320.

[20] G.J. Yao, S. Yang, J.R. He, S.J. Jiang, C.Z. Sun, S.Q. Song, In situ growing graphene on g-C3N4 with barrier-free interface and polarization electric field for strongly boosting solar energy conversion into H2 energy, Appl. Catal. B Environ. 287 (2021), 119986.

[21] X.L. Miao, X.Y. Yue, Z.Y. Jia, X.P. Shen, H. Zhou, M.M. Liu, K.Q. Xu, J. Zhu, G. X. Zhu, L.R. Kong, S.A. Shah, Nitrogen-doped carbon dots decorated on g-C3N4/Ag3PO4 photocatalyst with improved visible light photocatalytic activity and mechanism insight, Appl. Catal. B Environ. 227 (2018) 459–469.

[22] Y.Y. Jiao, Q.Z. Huang, J.S. Wang, Z.H. He, Z.J. Li, A novel MoS2 quantum dots (QDs) decorated Z-scheme g-C3N4 nanosheet/N-doped carbon dots heterostructure photocatalyst for photocatalytic hydrogen evolution, Appl. Catal. B Environ. 247 (2019) 124–132.

[23] F.L. Wang, Y.L. Wu, Y.F. Wang, J.H. Li, X.Y. Jin, Q.X. Zhang, R.B. Li, S.C. Yan, H. J. Liu, Y.P. Feng, G.G. Liu, W.Y. Lv, Construction of novel Z-scheme nitrogen-doped carbon dots/{0 0 1} TiO2 nanosheet photocatalysts for broad-spectrum-driven diclofenac degradation: mechanism insight, products and effects of natural water matrices, Chem. Eng. J. 356 (2019) 857–868.

[24] F.L. Wang, P. Chen, Y.P. Feng, Z.J. Xie, Y. Liu, Y.H. Su, Q.X. Zhang, Y.F. Wang, K. Yao, W.Y. Lv, G.G. Liu, Facile synthesis of N-doped carbon dots/g-C3N4 photocatalyst with enhanced visible-light photocatalytic activity for the degradation of indomethacin, Appl. Catal. B Environ. 207 (2017) 103–113.

[25] Y.L. Wu, F.L. Wang, X.Y. Jin, X.S. Zheng, Y.F. Wang, D.D. Wei, Q.X. Zhang, Y. P. Feng, Z.J. Xie, P. Chen, H.J. Liu, G.G. Liu, Highly active metal-free carbon dots/g-C3N4 hollow porous nanospheres for solar-light-driven PPCPs remediation: mechanism insights, kinetics and effects of natural water matrices, Water Res. 172 (2020), 115492.

[26] F. Yang, D.Z. Liu, Y.X. Li, L.J. Cheng, J.H. Ye, Salt-template-assisted construction of honeycomb-like structured g-C3N4 with tunable band structure for enhanced photocatalytic H2 production, Appl. Catal. B Environ. 240 (2019) 64–71.

[27] X.Y. Zhang, S. Zhang, Y. Yang, L.G. Wang, Z.J. Mu, H.S. Zhu, X.Q. Zhu, H.H. Xing, H.Y. Xia, B.L. Huang, J. Li, S.J. Guo, E.K. Wang, A general method for transition metal single atoms anchored on honeycomb-like nitrogen-doped carbon nanosheets, Adv. Mater. 32 (2020), 1906905.

[28] N. Díez, G.A. Ferrero, M. Sevilla, A.B. Fuertes, A sustainable approach to hierarchically porous carbons from tannic acid and their utilization in supercapacitive energy storage systems, J. Mater. Chem. A 7 (2019) 14280–14290.

[29] Z.F. Chen, S.C. Lu, Q.L. Wu, F. He, N.Q. Zhao, C.N. He, C.S. Shi, Salt-assisted synthesis of 3D open porous g-C3N4 decorated with cyano groups for photocatalytic hydrogen evolution, Nanoscale 10 (2018) 3008–3013.

[30] Z. Shu, Y. Wang, W.B. Wang, J. Zhou, T.T. Li, X.Q. Liu, Y.G. Tan, Z.L. Zhao, A green one-pot approach for mesoporous g-C3N4 nanosheets with in situ sodium doping for enhanced photocatalytic hydrogen evolution, Int. J. Hydrog. Energy 44 (2019) 748–756.

[31] F.L. Wang, T.T. Hou, X. Zhao, W. Yao, R.Q. Fang, K. Shen, Y.W. Li, Ordered macroporous carbonous frameworks implanted with CdS quantum dots for efficient photocatalytic CO2 reduction, Adv. Mater. 33 (2021), 2102690.

[32] D.D. Zheng, C.Y. Pang, Y.X. Liu, X.C. Wang, Shell-engineering of hollow g-C3N4 nanospheres via copolymerization for photocatalytic hydrogen evolution, Chem. Commun. 51 (2015) 9706–9709.

[33] Y. Bai, L.Q. Ye, L. Chen, L. Wang, X. Shi, X. Zhang, D. Chen, Facet-dependent photocatalytic N2 fixation of Bismuth-rich Bi5O7I nanosheets, ACS Appl. Mater. Interfaces 8 (2016) 27661–27668.

[34] M.H. Ai, J.W. Zhang, R.J. Gao, L. Pan, X.W. Zhang, J.J. Zou, MnOx-decorated 3D porous C3N4 with internal donor-acceptor motifs for efficient photocatalytic hydrogen production, Appl. Catal. B Environ. 256 (2019), 117805.

[35] Y.Y. Kang, Y.Q. Yang, L.C. Yin, X.D. Kang, G. Liu, H.M. Cheng, An amorphous carbon nitride photocatalyst with greatly extended visible-light-responsive range for photocatalytic hydrogen generation, Adv. Mater. 27 (2015) 4572–4577.

[36] G.H. Moon, M. Fujitsuka, S. Kim, T. Majima, X.C. Wang, W.Y. Choi, Eco-friendly photochemical production of H2O2 through O2 reduction over carbon nitride frameworks incorporated with multiple heteroelements, ACS Catal. 7 (2017) 2886–2895.

[37] S. Wu, H.T. Yu, S. Chen, X. Quan, Enhanced photocatalytic H2O2 production over carbon nitride by doping and defect engineering, ACS Catal. 10 (2020) 14380–14389.

[38] Y. Kofuji, S. Ohkita, Y. Shiraishi, H. Sakamoto, S. Tanaka, S. Ichikawa, T. Hirai, Graphitic carbon nitride doped with biphenyl diimide: efficient photocatalyst for hydrogen peroxide production from water and molecular oxygen by sunlight, ACS Catal. 6 (2016) 7021–7029.

[39] H.H. Ou, X.R. Chen, L.H. Lin, Y.X. Fang, X.C. Wang, Biomimetic donor-acceptor motifs in conjugated polymers forpromoting exciton splitting and charge separation, Angew. Chem. Int. Ed. 57 (2018) 8729–8733.

[40] Y.X. Li, S.X. Ouyang, H. Xu, W.S. Hou, M. Zhao, H.Y. Chen, J.H. Ye, Targeted exfoliation and reassembly of polymeric carbon nitride for efficient photocatalysis, Adv. Funct. Mater. 29 (2019), 1901024.

[41] J. Zhang, B. Xin, C. Shan, W.M. Zhang, D.D. Dionysiou, B.C. Pan, Roles of oxygen-containing functional groups of O-doped g-C3N4 in catalytic ozonation: quantitative relationship and first-principles investigation, Appl. Catal. B Environ. 292 (2021), 120155.

[42] Y.X. Li, H. Xu, S.X. Ouyang, D. Lu, X. Wang, D.F. Wang, J.H. Ye, In situ surface alkalinized g-C3N4 toward enhancement of photocatalytic H2 evolution under visible-light irradiation, J. Mater. Chem. A 4 (2016) 2943–2950.

[43] C.T. Guan, J. Jiang, S.Y. Pang, C.W. Luo, J. Ma, Y. Zhou, Y. Yang, Oxidation kinetics of bromophenols by nonradical activation of peroxydisulfate in the presence of carbon nanotube and formation of brominated polymeric products, Environ. Sci. Technol. 51 (2017) 10718–10728.

[44] W. Ren, L.L. Xiong, X.H. Yuan, Z.W. Yu, H. Zhang, X.G. Duan, S.B. Wang, Activation of peroxydisulfate on carbon nanotubes: electron-transfer mechanism, Environ. Sci. Technol. 53 (2019) 14595–14603.

[45] Y. Zhou, J. Jiang, Y. Gao, J. Ma, S.Y. Pang, J. Li, X.T. Lu, L.P. Yuan, Activation of peroxymonosulfate by benzoquinone: a novel nonradical oxidation process, Environ. Sci. Technol. 49 (2015) 12941–12950.

[46] Z.Y. Dong, Q. Zhang, B.Y. Chen, J.M. Hong, Oxidation of bisphenol A by persulfate via Fe3O4-α-MnO2 nanoflower-like catalyst: mechanism and efficiency, Chem. Eng. J. 357 (2019) 337–347.

[47] Y. Gao, X.G. Duan, B. Li, Q.Q. Jia, Y. Li, X.B. Fan, F.B. Zhang, G.L. Zhang, S. B. Wang, W.C. Peng, Fe containing template derived atomic Fe-N-C to boost Fenton-like reaction and charge migration analysis on highly active Fe-N4 sites, J. Mater. Chem. A 9 (2021) 14793–14805.

[48] P.P. Zhang, Y.Y. Yang, X.G. Duan, Y.J. Liu, S.B. Wang, Density functional theory calculations for insight into the heterocatalyst reactivity and mechanism in persulfate-based advanced oxidation reactions, ACS Catal. 11 (2021) 11129–11159.